

Optical and spectral observations and hydrodynamic modelling of Type IIb Supernova 2017gpn

Elena A. Balakina,^{1,2} Maria V. Pruzhinskaya,^{2,3}★ Alexander S. Moskvitin,⁴
Sergei I. Blinnikov,^{2,3,5,6} Xiaofeng Wang,^{7,8} Danfeng Xiang,⁷ Han Lin,⁷
Liming Rui⁷, and Huijuan Wang⁹

¹ Lomonosov Moscow State University, Faculty of Physics, Leninskie Gory, 1-2, Moscow, 119991, Russia

² Lomonosov Moscow State University, Sternberg Astronomical Institute, Universitetsky pr. 13, Moscow, 119234, Russia

³ Space Research Institute, 84/32 Profsoyuznaya Street, Moscow, 117997, Russia

⁴ Special Astrophysical Observatory RAS, Nizhnij Arhyz, 369167, Russia

⁵ NRC Kurchatov institute - ITEP, B. Cheremushkinskaya 25, 117218 Moscow, Russia

⁶ Kavli IPMU, University of Tokyo, Kashiwa, 277-8583, Japan

⁷ Physics Department and Tsinghua Center for Astrophysics, Tsinghua University, Beijing, 100084, China

⁸ Beijing Planetarium, Beijing Academy of Science and Technology, Beijing, 100044, China

⁹ National Astronomical Observatories, Chinese Academy of Sciences, Beijing, 100101, China

Accepted XXX. Received YYY; in original form ZZZ

ABSTRACT

In this work we present the photometric and spectroscopic observations of Type IIb Supernova 2017gpn. This supernova was discovered in the error-box of the LIGO/Virgo G299232 gravitational-wave event. We obtained the light curves in the *B* and *R* passbands and modelled them numerically using the one-dimensional radiation hydrocode STELLA. The best-fitting model has the following parameters: the pre-SN star mass and the radius are $M \approx 3.5 M_{\odot}$ and $R \approx 50 R_{\odot}$, respectively; the explosion energy is $E_{\text{exp}} \approx 1.2 \times 10^{51}$ erg; the mass of radioactive nickel is $M_{\text{Ni}} \approx 0.11 M_{\odot}$, which is completely mixed throughout the ejecta; and the mass of the hydrogen envelope $M_{\text{H,env}} \approx 0.06 M_{\odot}$. Moreover, SN 2017gpn is a confirmed SN IIb that is located at the farthest distance from the centre of its host galaxy NGC 1343 (i.e. the projected distance is ~ 21 kpc). This challenges the scenario of the origin of Type IIb Supernovae from massive stars.

Key words: supernovae: general – supernovae: individual: SN 2017gpn – stars: evolution

1 INTRODUCTION

Type IIb Supernovae (SNe IIb) are characterized by spectra evolving from dominant hydrogen lines at early times to increasingly strong helium features and progressively weaker hydrogen lines later on (Filippenko et al. 1993). This is the reason why SNe IIb are regarded as an intermediate group between hydrogen-rich SNe II and hydrogen-poor SNe Ib. SNe IIb are in the class of the stripped-envelope core-collapse supernovae (CCSNe). It is supposed that progenitors of such supernovae are massive stars that have lost most of their hydrogen envelope (Clocchiatti & Wheeler 1997).

Nowadays there are two hypotheses explaining how stars can lose the hydrogen envelope. The first scenario supposes the evolution of a rather massive $M \approx 25 M_{\odot}$ single star with an average mass-loss rate of about $10^{-5} M_{\odot}$ per year. Such a powerful stellar wind could provide the required outflow of hydrogen (Hoflich et al.

1993). The second and more plausible scenario involves a mass transfer in a binary system where the progenitor star is a supergiant of moderate mass (Nomoto et al. 1993; Woosley et al. 1994; Bersten et al. 2012). The massive companion expands and fills its Roche lobe, after which mass transfer starts due to Roche-lobe overflow (Yoon et al. 2017).

Nevertheless, the progenitor nature of SNe IIb is still not clear. While SNe II form a continuous group as Anderson et al. (2014) and Sanders et al. (2015) established, Pessi et al. (2019) showed that SN II light curves are distinct from those of SNe IIb with no suggestion of a continuum distribution. This fact suggests that progenitors of SNe IIb make up a separate group that is different from the SNe II ones. However, it could also be a consequence of the lack of observational data: SNe IIb make up less than 5 per cent of all CC-SNe according to the Open Supernova Catalog¹ (Guillochon et al. 2017) and only about two dozen of them have detailed multicolour

★ E-mail: pruzhinskaya@gmail.com

¹ <https://sne.space>

photometry appropriate for further study (including hydrodynamic modelling).

To extend the sample of well-studied SNe IIB, in this paper we present the photometric and spectroscopic observations of SN 2017gpn. The photometry was performed with the Zeiss-1000 telescope (Komarov et al. 2020) at the Special Astrophysical Observatory of the Russian Academy of Science (SAO RAS). Spectroscopic data were obtained with the Xinglong 2.16-m telescope at the National Astronomical Observatory of China. Collected photometric data are used for the numerical light-curve (LC) calculations done by the radiation hydrocode STELLA (Blinnikov et al. 1998, 2006). These simulations give us the parameters of the pre-supernova star and explosion characteristics.

The interest in this supernova is also augmented by the fact that we usually only observe such supernovae in spiral galaxies in hydrogen-rich environments where young massive stars are being born (Filippenko 1997). In contrast to this, SN 2017gpn is located quite far from the active star-formation regions and the spiral arms of the host galaxy. We also do not see any dwarf satellite galaxies at the SN location. The unusual location of SN 2017gpn in the host galaxy indicates that the existing models of SN IIB progenitors may not explain all observational data and have to be reviewed.

This paper is organized as follows. In Section 2 we describe the observations, data processing, and resulting light curves and spectra. In Section 3 we present the hydrodynamic modelling of SN 2017gpn and the parameters of the best-fitting model. Section 4 contains a comparison of the modelling results, LC behaviour, and spectral features of SN 2017gpn with those for other SNe IIB and a discussion of the unexpected location of SN 2017gpn relative to its host galaxy. Finally, we conclude the paper in Section 5.

2 OBSERVATIONS

2.1 Discovery

On the last day of the second advanced detector observing run “O2”, the LIGO/Virgo Collaboration released the G299232 alert². During the follow-up inspection of the gravitational-wave (GW) candidate error-box, on 2017 August 27.017 the MASTER Global Robotic Net (Lipunov et al. 2010) discovered an optical transient named MASTER OT J033744.97+723159.0 (Lipunov et al. 2017).

On the discovery day, three spectra of MASTER OT J033744.97+723159.0 were obtained with the ACAM instrument mounted on the William Herschel Telescope at La Palma (Spain) by Jonker et al. (2017) and the analysis showed that the transient classifies as SNe IIB. Further observations on 2017 August 29 obtained with the SPRAT spectrograph on the Liverpool Telescope (Copperwheat et al. 2017) and with the Xinglong 2.16-m telescope of the National Astronomical Observatory of China (Rui et al. 2017; Wang 2017) confirmed this classification by cross-correlating with a library of spectra with use of the Supernova Identification code (SNID; Blondin & Tonry 2007). According to SNID, the spectrum with the highest correlation coefficient belongs to Type IIB SN 1996cb at phase -2 d.

On 2017 September 6 at 03:21:12 UT, Caimmi (2017) reported the discovery of a supernova with the 0.24-m telescope from the Valdicerro Observatory. The supernova received the IAU designation AT 2017gpn and was identified as MASTER OT J033744.97+723159.0.

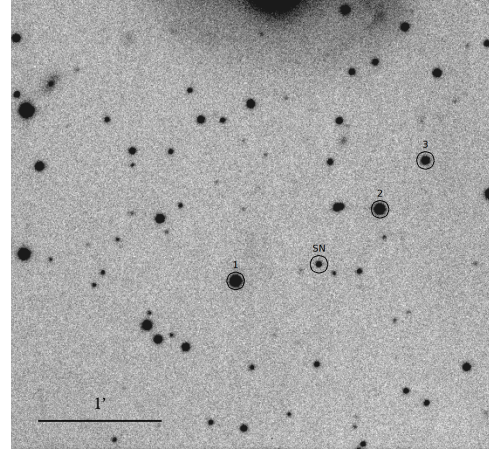


Figure 1. SN 2017gpn and comparison stars. The image is obtained with the Zeiss-1000 telescope in R passband.

Table 1. Magnitudes of the comparison stars in the B and R passbands derived from g, r, i Pan-STARRS1 magnitudes using Lupton’s 2005 transformation equations.

No	B	err_B	R	err_R
1	16.447	0.011	15.032	0.015
2	16.859	0.012	15.428	0.015
3	17.705	0.011	16.636	0.017

SN 2017gpn is located ~ 140 arcsec from the centre of the host galaxy NGC 1343 (Fig. 1). Taking into account that the redshift of NGC 1343 is 0.0073 (Springob et al. 2005) and assuming flat Λ CDM cosmology with $\Omega_\Lambda = 0.7$ and $H_0 = 70 \text{ km s}^{-1} \text{ Mpc}^{-1}$, we find that the projected distance between SN 2017gpn and the centre of its host is ~ 21 kpc.

2.2 Photometric data processing

We performed 20 epochs of observations (B and R passbands) with the CCD photometer on the Zeiss-1000 telescope at SAO RAS. The aperture photometry was performed using standard procedures of the ESO MIDAS software package. It includes standard image processing such as bias subtraction and flat field correction, removing the traces of cosmic particles, and stacking of individual frames into a summary image.

Since no Landolt or any other standards (Stetson 1987; Landolt 1992) were available for this region, we use the Pan-STARRS (Chambers et al. 2016; Flewelling et al. 2016) magnitudes for comparison stars. These magnitudes were recalculated from the g, r, i passbands to B and R with the use of Lupton’s transformation equations³:

$$\begin{aligned}
 B &= g + 0.3130 (g - r) + 0.2271, & \sigma &= 0.0107 \\
 R &= r - 0.1837 (g - r) - 0.0971, & \sigma &= 0.0106 \\
 R &= r - 0.2936 (r - i) - 0.1439, & \sigma &= 0.0072
 \end{aligned} \tag{1}$$

² <https://gcn.gsfc.nasa.gov/other/G299232.gcn3>

³ <http://www.sdss3.org/dr8/algorithms/sdssUBVRITransform.php>

Table 2. Photometric observations of SN 2017gpn with the Zeiss-1000 telescope. The magnitudes are corrected for the expected Galactic foreground extinction.

JD 2457990+	<i>B</i>	err _{<i>B</i>}	<i>R</i>	err _{<i>R</i>}
21.5	16.65	0.07	15.34	0.03
22.5	16.75	0.05	15.41	0.02
25.6	17.08	0.05	15.58	0.03
26.5	17.16	0.05	15.62	0.04
27.5	17.24	0.06	15.67	0.02
28.5	17.33	0.06	15.73	0.02
29.6	17.35	0.05	15.81	0.02
31.5	17.44	0.06	15.88	0.03
56.4	17.90	0.06	16.62	0.02
57.4	17.89	0.05	16.63	0.01
76.5	—	—	17.17	0.03
77.4	18.17	0.07	17.13	0.03
78.6	18.14	0.06	17.21	0.03
85.6	18.22	0.05	17.21	0.03
107.6	—	—	18.06	0.04
110.4	18.61	0.07	17.89	0.03
143.3	19.14	0.15	18.78	0.01
153.3	—	—	18.54	0.30
224.3	—	—	21.14	0.20

The comparison stars are shown in Fig. 1 and their magnitudes are listed in Table 1.

We use a line-of-sight reddening for our Galaxy of $E(B - V) = 0.30$ mag (Schlafly & Finkbeiner 2011), corresponding to additive magnitude corrections of 1.246 and 0.725 mag for the *B* and *R* passbands, respectively. Since SN 2017gpn is very far from the centre of NGC 1343, we assume that the host's contamination is negligible. The resulting photometric data are presented in Table 2.

2.3 Resulting light curves

With Zeiss-1000 observations we can restore only the post-maximum part of the light curve. This is why, to improve the accuracy of the further hydrodynamic modelling (see Section 3), we supplemented our data with observations in the *B* and *R* passbands from Roberts & Kolb 2018 obtained with the PIRATE robotic telescope in Spain (Holmes et al. 2011). The resulting light curve is presented in Fig. 2. The data points obtained at Zeiss-1000 (shown as circles) and the data points taken from Roberts & Kolb 2018 (marked with crosses) mutually complement each other and allow us to restore the *B* and *R* light curves almost entirely.

One can notice a slight shift between the two data sets. This may be due to the different sources of photometry for the comparison stars since there are no Stetson and Landolt photometric standards in this field. However, the difference between the values is less than the uncertainty associated with the choice of hydrodynamic model; therefore for our purpose it can be neglected.

2.4 Spectra

The spectroscopic observations were collected using the Xinglong 2.16-m telescope and the BFOSC system. All the spectra were reduced using routine tasks within IRAF and the flux was calibrated with spectrophotometric standard stars observed on the same nights. Telluric lines are removed from all of these spectra. The journal of our spectroscopic observations is given in Table 3.

Three optical spectra were obtained for SN 2017gpn, covering

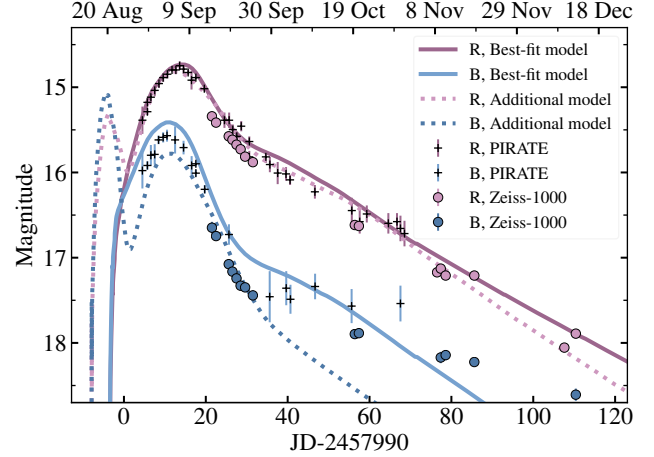


Figure 2. Light curve of SN 2017gpn. Pink and blue solid lines correspond to the best-fitting model; dashed lines to the additional model in the *R* and *B* passbands, respectively. Circles are the Zeiss-1000 data; crosses are the data taken from Roberts & Kolb 2018.

the phases from -8.3 to $+19.7$ d from the *R*-band maximum light (peak time is $\text{JD} = 2458003.6$); these are shown in Fig. 3. At one week before the peak, the spectrum shows strong Balmer lines of hydrogen, providing evidence of a Type II Supernova. Moreover, the existing prominent absorption features at ~ 5670 and 6860 Å that can be identified as $\text{He I } \lambda 5876$ and $\text{He I } \lambda 7065$, respectively, confirming that SN 2017gpn can be further put into the Type IIb subclass. From the absorption minima of $\text{H } \alpha$ and $\text{He I } \lambda 5876$ lines at the first obtained spectrum, we measured the ejecta velocity as 15000 ± 130 and 10100 ± 300 km s^{-1} , respectively, indicating that the Balmer lines and the He I lines originated from different layers (see Table 3). At two weeks after the maximum, the helium features seem to become more noticeable and other helium features such as $\text{He I } \lambda 6678$ (blueshifted to ~ 6510 Å) emerge in the spectrum. The helium features become even more pronounced in the spectrum taken one week later, while the hydrogen features become gradually weaker. The overall spectral evolution of SN 2017gpn is presented in Fig. 3 and it is similar to other typical Type IIb Supernovae, like SN 1993J (Barbon et al. 1995), SN 1996cb (Qiu et al. 1999), and SN 2008ax (Modjaz et al. 2014).

3 MODELLING

3.1 Pre-supernova models

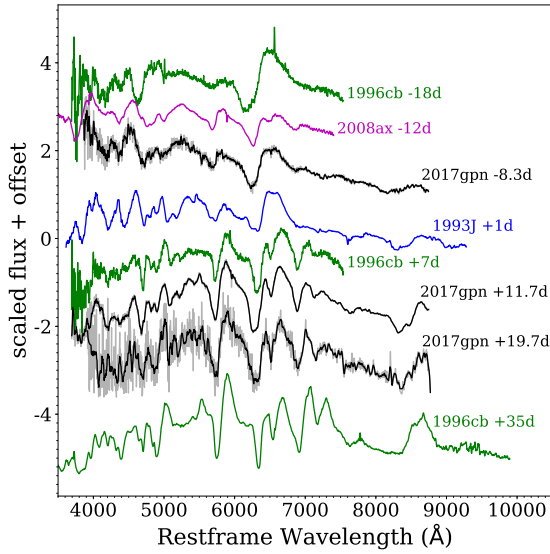
A set of non-evolutionary pre-supernova models is obtained under the assumption of a power-law dependence of temperature on density: $T \propto \rho^\alpha$ (Nadyozhin & Razinkova 1986; Blinnikov & Bartunov 1993). Therefore, the obtained hydrostatic configuration would be close to a polytrope of index $1/\alpha \approx 3$. The deviation from the polytropic model increases in the outer layers due to recombination of ions and non-homogeneous chemical composition.

At the centre of such a configuration we isolated a point-like source of gravity that has a non-negligible influence on the expansion of the innermost layers of supernova ejecta. The mass and radius of this compact remnant are taken as $M_{\text{CR}} = 1.41 M_\odot$ and $0.01 R_\odot$ for all treated pre-SN models.

In our approach we do not follow the explosive nucleosynthesis. Thus, the SN ejecta composition is the same as the pre-SN

Table 3. Journal of spectroscopic observations of SN 2017gpn with the BFOSC+G4 instrument of the Xinglong 2.16-m telescope. Values of the ejecta velocity measured from the absorption lines of H α , He I λ 5876, Fe II λ 5018, and Fe II λ 5169 are also presented.

JD 2457990+	Exp. Time [s]	H α [km s ⁻¹]	He I λ 5876 [km s ⁻¹]	Fe II λ 5018 [km s ⁻¹]	Fe II λ 5169 [km s ⁻¹]
5.30	3600	15000 \pm 130	10100 \pm 300	12000 \pm 1200	11400 \pm 950
25.29	3600	13200 \pm 100	8000 \pm 100	6750 \pm 470	5130 \pm 490
33.33	2700	12900 \pm 200	7300 \pm 200	—	—

**Figure 3.** Three spectra of SN 2017gpn at different phases, the observation dates are indicated with respect to the R -band maximum light at JD = 2458003.6. Spectra of SNe IIb 1993J, 1996cb, and 2008ax are presented for comparison.

composition except for ^{56}Ni . Since the amount and distribution of ^{56}Ni synthesized during the explosion plays a crucial role in the SN luminosity evolution, we consider two radial distributions for ^{56}Ni . In the first one ^{56}Ni is totally mixed through the ejecta and in the second one ^{56}Ni falls off from the centre.

As input parameters for further hydrodynamical modelling, we varied the pre-SN star mass M and the radius R , the mass of synthesized nickel $M_{^{56}\text{Ni}}$, and the initial distribution of chemical elements in the pre-SN star.

3.2 STELLA code

To explode the hydrostatic non-evolutionary pre-SN models a one-dimensional multifrequency radiation hydrocode STELLA is used. The full description of the code can be found in Blinnikov et al. (1998, 2006); a public version of STELLA is also included with the MESA distribution (Paxton et al. 2018). The STELLA code is used for the light-curve modelling of different types of SNe — Ia (Blinnikov et al. 2006), Ib/Ic (Folatelli et al. 2006; Tauris et al. 2013), IIb (Blinnikov et al. 1998; Tsvetkov et al. 2012), IIc (Chugai et al. 2004), IIP (Baklanov et al. 2005; Tominaga et al. 2009), Ic associated with long gamma-ray bursts (Volnova et al. 2017). The

Table 4. Parameters for the best-fitting and additional hydrodynamic models of SN 2017gpn.

Parameter	Best-fitting model	Additional model
R	50 R_{\odot}	400 R_{\odot}
M	3.5 M_{\odot}	3.5 M_{\odot}
$M_{\text{H,env}}$	0.06 M_{\odot}	0.21 M_{\odot}
M_{CR}	1.41 M_{\odot}	1.41 M_{\odot}
$M_{^{56}\text{Ni}}$	0.11 M_{\odot} , mixed	0.11 M_{\odot} , no mixing
E_{exp}	1.2×10^{51} erg	1.2×10^{51} erg
$t_{\text{peak},R}$	2017 Sept 7.5	2017 Sept 5.6

STELLA code was compared with other well-known hydrodynamic codes and found to be in good agreement with them on the level of several per cent (e.g. Woosley et al. 2007; Kromer & Sim 2009; Sim et al. 2010; Kozyreva et al. 2017; Tsang et al. 2020).

In the current calculations, we adopted 100 zones for the Lagrangian coordinate and 130 frequency bins. The explosion is initiated by putting thermal energy into the innermost layers. The energy is released in 0.1 s, which is less than the hydrodynamic time of the pre-supernova. While this condition is true, the resulting light curve is not affected by the details of the explosion mechanism (Imshennik & Nadezhin 1983).

3.3 Best-fitting model

To determine the best-fitting model of SN 2017gpn we consider a grid of parameters. The pre-SN mass varies between 3.5 M_{\odot} and 5.5 M_{\odot} with steps of 0.5 M_{\odot} ; the pre-SN radius and E_{exp} take the values {50, 100, 200, 400, 600} R_{\odot} and {0.6, 1.2, 2.4} $\times 10^{51}$ erg, respectively; three different $M_{^{56}\text{Ni}}$ {0.07, 0.09, 0.11} M_{\odot} are considered, both with and without mixing. The mass of the hydrogen envelope $M_{\text{H,env}}$ is taken as 0.06 M_{\odot} which is in line with our expectations for Type IIb Supernovae.

After determination of the parameter grid we built trial models and chose the best-fitting model within the generated grids of light curves by calculating χ^2 in the R passband. The best-fitting model corresponds to the minimum value of χ^2 . We do not provide any statistical uncertainties, since this procedure requires enormous computational effort. Instead, the optimal model is recovered as a compromise between the fits to the observed light curve and the evolution of the velocity at the photosphere (see Section 4.2.1). The values of the best-fitting model parameters are summarized in Table 4. Fig. 2 compares the light curves of the model (solid lines) with the observations of SN 2017gpn.

In Fig. 4 we also show the distribution of the chemical elements and the density profile for a pre-SN star. Note that the best-fitting model shows a small amount of hydrogen in the pre-SN star composition, which is expected for SNe IIb (Filippenko et al. 1993). ^{56}Ni is totally mixed through the ejecta.

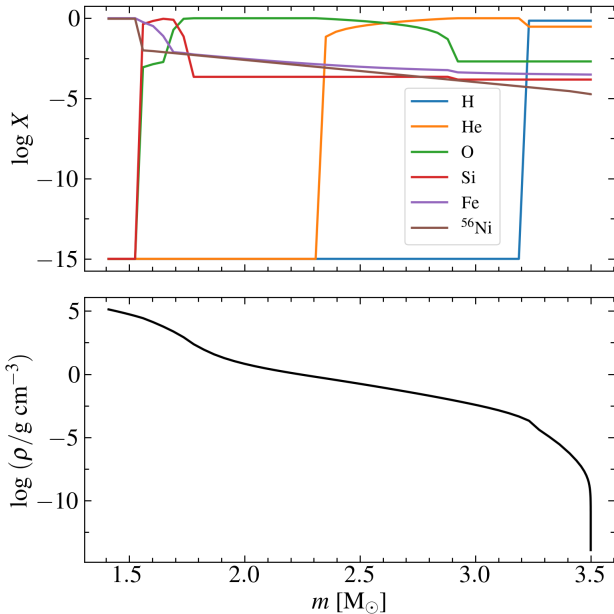


Figure 4. Mass fractions of the most abundant chemical elements in the ejecta (top) and density profile (bottom) for the best-fitting pre-SN star model with respect to the interior mass. The central region of $1.41 M_\odot$ is taken away.

3.4 The influence of the model parameters on the light curve

To provide a reasonable range of the best-fitting model parameters, we consider the dependence of the numerical LCs on an input parameter of the model while the others remain fixed. We vary the mass M and the radius R of the pre-SN star, the mass of synthesized ^{56}Ni , and the energy of the explosion E_{exp} . In Fig. 5 we plot some modelled LCs in the R passband that show a valid range for each parameter. All presented models are slightly shifted along the time axis to better describe the observational light curve.

The first considered parameter is the pre-SN mass M , see Fig. 5 (a). This parameter mainly affects the width of the light curve, which becomes broader as the mass increases. This is explained by the fact that with a small mass the envelope becomes transparent faster. Thus, the LC increases before the maximum light and decreases rapidly after it. As Fig. 5 (a) shows, the range of valid pre-SN mass is $3\text{--}4 M_\odot$.

The next parameter is the amount of synthesized ^{56}Ni (Fig. 5 (b)). The models are brighter for higher ^{56}Ni masses. The LCs corresponding to the ^{56}Ni masses of 0.09 and $0.13 M_\odot$ lie below and above the best-fitting model light curve, respectively. These two values define the acceptance range of the $M_{^{56}\text{Ni}}$ model parameter.

The pre-SN radius affects mainly the light-curve tail: a larger radius value corresponds to a brighter light curve after maximum light. The chosen range of the pre-SN radius is $20\text{--}70 R_\odot$; see Fig. 5 (c).

The last parameter that we vary is the explosion energy E_{exp} ; see Fig. 5 (d). The determined range for the energy parameter is $(1.05\text{--}1.60) \times 10^{51}$ erg. As seen from Fig 5 (d), smaller values of E_{exp} correspond to brighter light curves. This dependence is in line with our expectations. A larger E_{exp} , for a fixed mass of ^{56}Ni and fixed total mass, implies higher velocities and hence less trapping of

gamma-ray photons. This leads to an increase in the predicted observed gamma-ray flux and, therefore, to a decrease in the emission in the visible light range.

4 DISCUSSION

4.1 Comparison with other SNe I Ib

We collected data for well-studied SNe I Ib with good photometric coverage in the B and R passbands, for which results of hydrodynamic modelling can be found in the literature. In Fig. 6 the light curves of selected SNe I Ib are presented. It can be seen that LCs in the B and R passbands are similar — characteristic bell-shaped LCs. Moreover, as Pessi et al. (2019) showed, SNe I Ib take longer to reach maximum light and decline more quickly post-maximum than hydrogen-rich SNe II, so the authors assume that there is no continuum between SNe I Ib and other SNe II like between SNe IIP and IIL types. SN 2017gpn has a typical SN I Ib light curve, and belongs to one of the brightest well-studied SNe I Ib: it is brighter than a typical member of Type I Ib SN 1993J by 0.75 mag in the R passband.

4.1.1 Classification of Prentice & Mazzali (2017)

Following Prentice & Mazzali (2017), stripped-envelope SNe should be subclassified into four groups: Ib, Ib(II), I Ib, and I Ib(I), using the additional parameters — equivalent width of $H \alpha$ ($EW_{H \alpha}$) and $H \alpha$ emission-to-absorption ratio $f_{\text{em}}/f_{\text{abs}}$. The $EW_{H \alpha}$ parameter value is $> 60 \text{ \AA}$ for supernovae of group I Ib(I), $20 < EW_{H \alpha} < 60 \text{ \AA}$ for Ib(II), and takes any reasonable value for groups Ib and I Ib. The $H \alpha$ emission-to-absorption ratio $f_{\text{em}}/f_{\text{abs}}$ differs for groups Ib and I Ib(I): it ranges from $0.3\text{--}1$ for I Ib(I) and is greater than 1 for group Ib (see Fig. 7).

We calculated the intensity and equivalent width of $H \alpha$ in our first spectrum (-8.3 d before R -band maximum) for SN 2017gpn and found $f_{\text{em}}/f_{\text{abs}} = 0.63 \pm 0.04$, $EW_{H \alpha} = 123 \pm 3 \text{ \AA}$. Therefore, SN 2017gpn belongs to group I Ib(I) which means that it might have less hydrogen in the envelope than most H-rich SNe such as 1993J, 2011fu, or 2011dh (see Table 5). However, it is similar to other SNe I Ib(I) — 2008ax and 1996cb (the first position in a cross-correlation list according to SNID).

4.1.2 Hydrodynamic models of other SNe I Ib

We compare the results of numerical simulations for SN 2017gpn and other SNe I Ib (including groups Ib and I Ib(I) of Prentice & Mazzali 2017) presented in Fig. 6. Only hydrodynamic modelling of supernovae is chosen for comparison; we do not consider any analytical light-curve modelling or scaling to templates. The modelling results are summarised in Table 5, where M_{CR} is the mass of a compact object (generally this is a neutron star) and M_{ej} is the mass of ejected matter.

The main modelling parameters such as the ejecta mass M_{ej} , the mass of ^{56}Ni , $M_{\text{H,env}}$, and the explosion energy E_{exp} are consistent with each other. An exception is the parameter of the pre-supernova radius R . The considered hydrodynamic modelling shows that the pre-SN radius lies in a broad range from $30\text{--}720 R_\odot$ and may be different for the same object in different models. For example, there are two models for SN 2008ax, one with a radius of $30\text{--}50 R_\odot$ (Folatelli et al. 2015) and another one with $R = 600 R_\odot$ (Tsvetkov et al. 2009). It should be noted

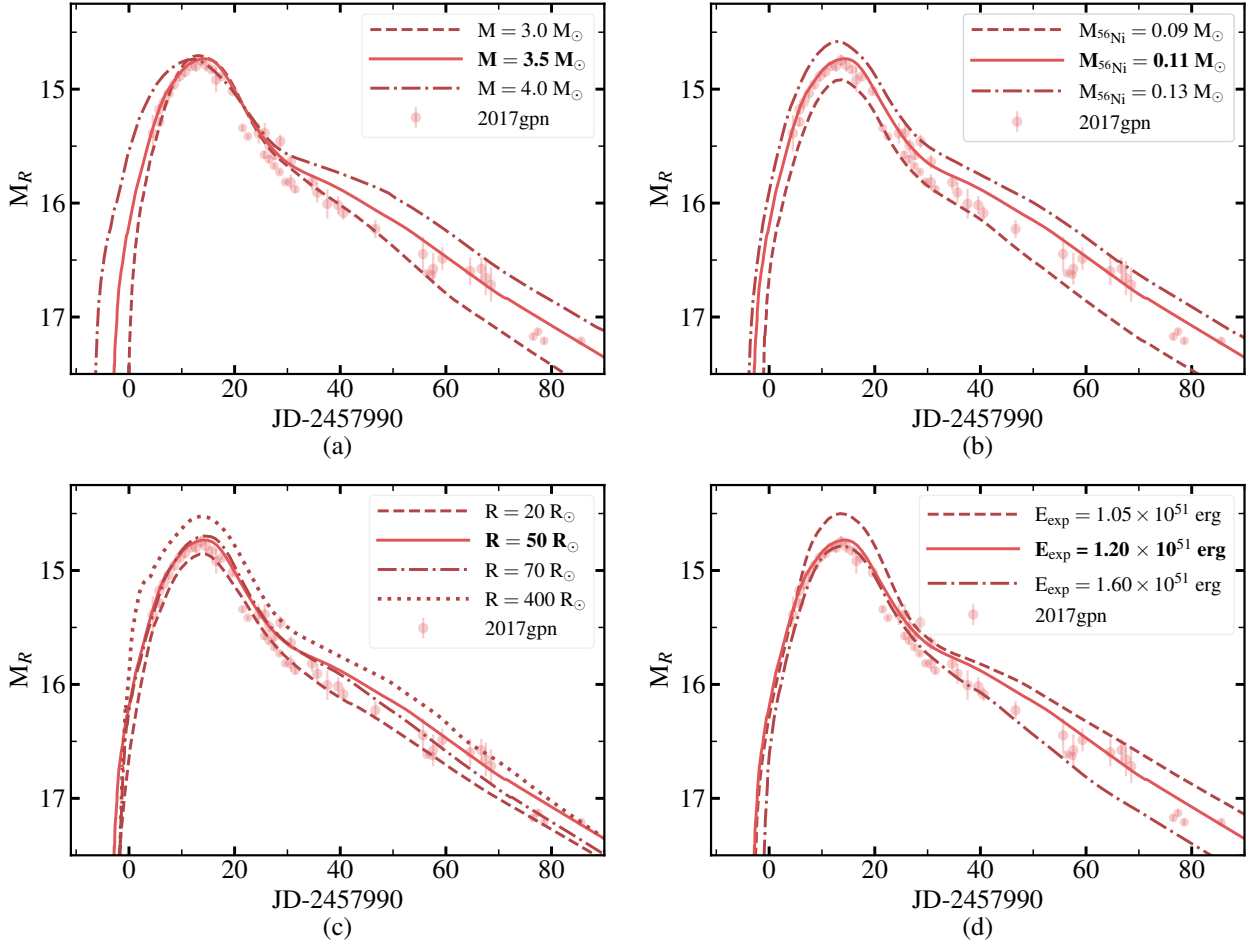


Figure 5. The dependence of the modelled R -passband LC on the pre-SN mass M (a), the amount of synthesized ^{56}Ni (b), the pre-SN radius R (c), and the explosion energy E_{exp} (d). All models are shifted along the time axis to better describe the observations. The best-fitting model is shown by a solid line in all plots; observations are shown by circles.

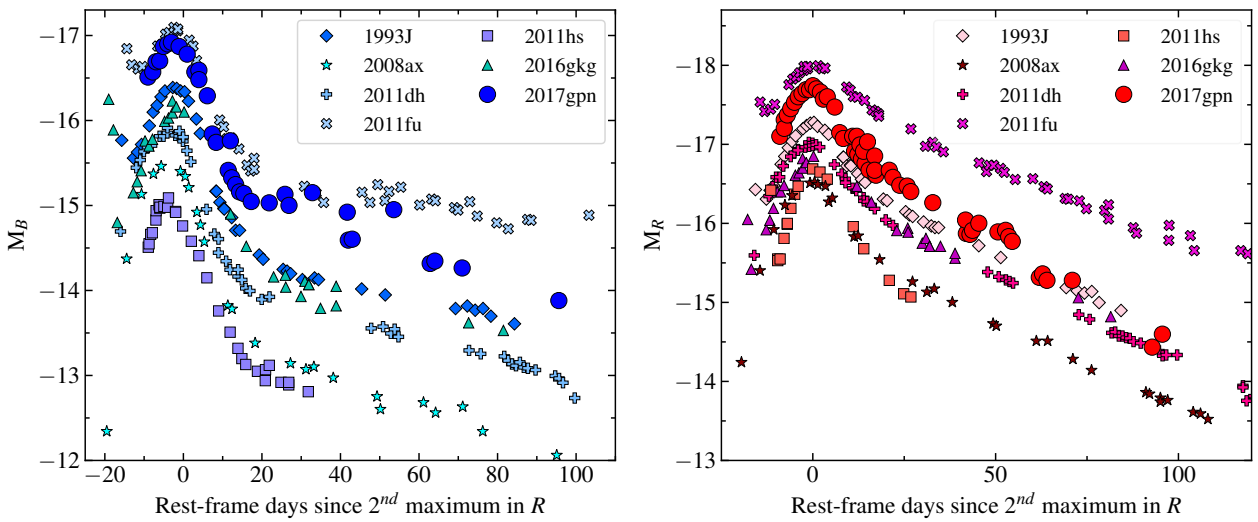


Figure 6. M_B and M_R light curves of SN 2017gpn in comparison with those of other Type IIb Supernovae: 1993J (Richmond et al. 1996), 2008ax (Tsvetkov et al. 2009), 2011dh (Tsvetkov et al. 2012), 2011fu (Kumar et al. 2013), 2011hs (Bufano et al. 2014), 2016gkg (Bersten et al. 2018).

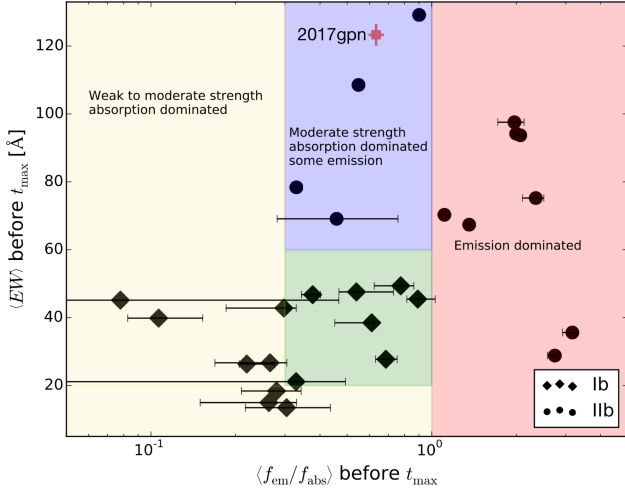


Figure 7. This figure is borrowed from [Prentice & Mazzali 2017](#) (fig. 7) with SN 2017gpn plotted (pink square). It illustrates the stripped-envelope supernovae subclassification based on the comparison of the line strength (equivalent width of H α) against the line profile (H α emission-to-absorption ratio f_{em}/f_{abs}) as proposed by [Prentice & Mazzali \(2017\)](#). SN 2017gpn lies in the blue region that corresponds to group IIb(I). Groups IIb, Ib, and Ib(II) are in the red, yellow, and green regions, respectively.

that SN 2008ax belongs to the same group of IIb(I) supernovae as SN 2017gpn.

4.2 Additional model

Motivated by the discrepancy in the modelled radius for different SNe IIb, we have found another physically reasonable model for SN 2017gpn with $R = 400 R_{\odot}$. For this additional model, radioactive nickel is located in the central part of the ejecta. We have also increased the mass of the hydrogen envelope to $0.21 M_{\odot}$, which is consistent with the fact that more extended SNe IIb should be also more H-rich ([Prentice & Mazzali 2017](#)). The parameters of the additional model are listed in Table 4. This model also well describes the observational data and agrees with the results of the hydrodynamic simulations for other SNe IIb.

There is no direct method to solve the inverse problem, i.e. to determine the parameters of the pre-supernova from the observational data. We can only build a model with given parameters and see how accurately it fits the data. Sometimes it can happen that models with different parameters reproduce observations equally well, as we see for our best-fitting and additional models (Fig. 2). However, if some additional information is available, e.g. observational photospheric velocities, we can compare our theoretical estimations with the observational values and make a choice between the models.

4.2.1 Photospheric velocities

Based on three spectra of SN 2017gpn obtained at different epochs with the Xinglong 2.16-m telescope, we measured the ejecta velocity from the H α and He I $\lambda 5876$ absorption lines (Table 3). In Fig. 8 we show the comparison between the velocities measured from these lines and theoretical values from the STELLA code, which are the velocities of the photosphere at the $\tau = 2/3$ level in the B band. The best-fitting model is consistent with the velocity

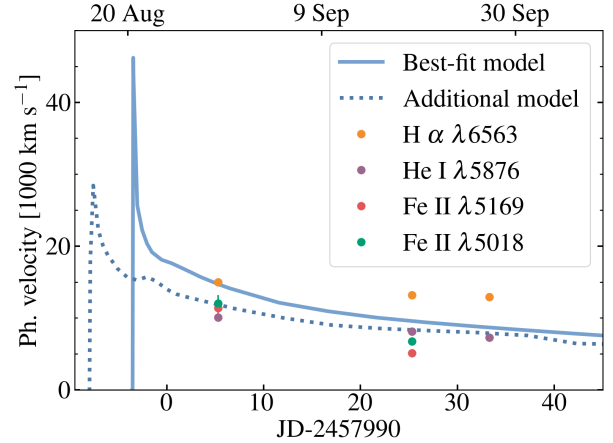


Figure 8. Photospheric velocity at the $\tau = 2/3$ level as a function of time for the best-fitting model (solid line) and for the additional model of higher radius (dashed line); dots are the observational velocities measured from the H α , He I $\lambda 5876$, Fe II $\lambda 5018$, and Fe II $\lambda 5169$ absorption lines.

measured from the H α line for this epoch; the additional model is in good agreement with the He I $\lambda 5876$ velocities for all three epochs.

It should be noted that P Cygni profiles are formed in all layers above the photosphere. Hence, the hydrogen and helium features do not necessarily reflect the photospheric velocities calculated by our hydrodynamic modelling. It has to be taken into account that the growth of the Sobolev optical depth ([Sobolev 1960](#)) at the photosphere level causes a significant blueshift of the P Cygni profile minimum, so the resulting velocity in that case will be overestimated ([Kasen et al. 2002](#)). This effect may explain why the velocities measured from the H α line are greater than our theoretical estimates in Fig. 8. Meanwhile, according to [Dessart & Hillier 2005, 2006](#) the velocities measured from strong lines can be both smaller and larger than the photospheric ones.

Therefore, it is more reasonable to use “weak” lines, i.e. lines with small Sobolev optical depths, to estimate v_{ph} . ([Dessart & Hillier 2005](#)) show that Na I D, Fe II $\lambda 5018$, Fe II $\lambda 5169$ are the most suitable lines to measure the photospheric velocities. We measured the velocities from the Fe II $\lambda 5018$ and 5169 lines for the first and second epochs of observations, the last epoch spectrum has a low signal-to-noise ratio to perform the measurements. We could not determine the velocities using Na I D features since they are close to He I $\lambda 5876$ line, which is quite strong in SNe IIb.

The photospheric velocities derived for the additional model correspond slightly better to the velocities from the Fe II $\lambda 5018$ and 5169 lines for the first epoch of observations. For the second epoch the measured velocities are lower than the STELLA values for both models. Taking into account the modelling uncertainties, it is difficult to choose between the models based on these measurements only.

4.2.2 ^{56}Ni mixing

From the theoretical bolometric LCs (Fig. 9) as well as LCs in filters (Fig. 2) it can be noticed that the light curve corresponding to the model with the uniform distribution of nickel behaves differently from the light curve that conforms with the model where nickel is concentrated in the centre of the ejecta. This is due to the fact that in the former case the radioactive decay energy contributes to the overall energy immediately after the explosion, whereas in the latter

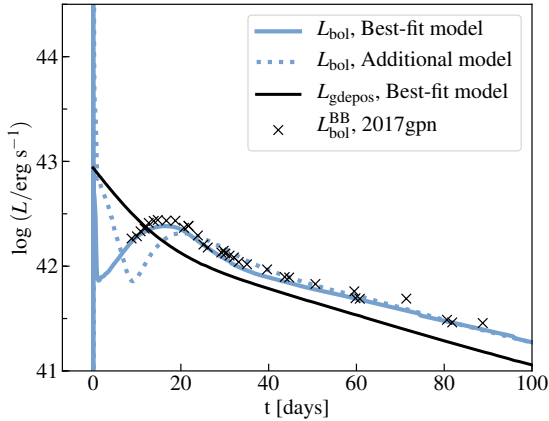


Figure 9. Theoretical bolometric light curves for the best-fitting (blue solid line) and the additional (blue dashed line) models of SN2017gpn. The crosses show the bolometric luminosity of SN 2017gpn calculated from *B* and *R* light curves with use of the SUPERBOL code (Nicholl 2018). The shift between the data and the best-fitting model is the same as in Fig. 2 but transformed to the rest frame. The black solid line is the power due to the gamma-ray deposition from ^{56}Ni and ^{56}Co decays for our best-fitting model. Accounting for the light travel time correction, L_{gdepos} satisfies Arnett’s law, going through the maximum of L_{bol} .

case we observe two peaks in the light curve. The primary peak is associated with the heating of the outer layers of the star by the shock wave that is created by the rebound of the freely falling inner layers from the collapsed core. After that the envelope expands, cools, and therefore becomes transparent. The second peak is associated with the luminescence of the inner layers heated by the radioactive decays of ^{56}Ni and its products. For the additional model we fit the observed LCs by the second peak. Because of this, the best-fitting and additional models are shifted relative to each other in Fig. 2. The influence of ^{56}Ni mixing on the LC behaviour is also seen if we compare the additional model with the model in Fig 5 (c) (dotted line) with $R = 400 R_{\odot}$ and ^{56}Ni totally mixed through the ejecta. Unlike the additional model, this model no longer describes the observations.

In Fig. 9 we also show the bolometric light curve of SN 2017gpn restored from the available photometry. To construct the bolometric light curve the SUPERBOL code is used (Nicholl 2018). To account for flux that is not covered by the observations, the black light extrapolation is applied. Even though we use only two passbands (*B* and *R*) the obtained bolometric LC agrees very well with our theoretical estimations.

4.3 Arnett’s law

Arnett’s law (Arnett 1982) states that the energy released on the surface at maximum light is equal to the energy deposited by gamma-ray radiation. This law is commonly used to estimate the amount of nickel produced in the explosion when the total luminosity at peak is known (Branch 1992). We plot the theoretical bolometric light curve and the curve corresponding to gamma-ray deposition from ^{56}Ni and ^{56}Co decays for our best-fitting model to check this law. As we can see from Fig. 9, the law is quite well satisfied; however, the power from gamma-ray deposition does not go directly through the L_{bol} peak. This is explained by the fact that Arnett’s law is not exact and in particular assumes an infinite speed of light. In the STELLA

code the energy released in the centre will be “seen” with a delay of R/c , where R is the radius of the expanding ejecta that changes with time and c is the speed of light. The observed difference increases towards the tail since the radius increases as well.

4.4 SN 2017gpn position relative to the host galaxy centre

Supernova 2017gpn exploded in the spiral galaxy NGC 1343 at a projected distance of $D \approx 21$ kpc from its centre (see Fig. 1). Such location is unusual for core-collapse supernovae, in particular for Type IIb, since it is believed that stripped-envelope CCSNe are formed from very massive stars in star-formation regions of galaxies (see Audcent-Ross et al. 2020 and references therein). Assuming that SN 2017gpn belongs to the galactic disk we can take into account the projection effect. The deprojected distance D_{dep} between the supernova and the host centre is calculated as

$$D_{\text{dep}} = D \sqrt{\cos^2 \alpha + \sin^2 \alpha \sec^2 i}, \quad (2)$$

where α is the angle between the projected distance and the major axis of a galaxy and i is the disc inclination angle. According to HyperLEDA i equals 67.3 deg and the major axis position angle of NGC 1343 is 78.8 deg (Makarov et al. 2014). Using these values and the coordinates of SN 2017gpn and its host galaxy centre we can calculate the deprojected distance for SN 2017gpn, which is ~ 52 kpc. To understand how exceptional this position is we study the absolute and relative separations between the supernova positions and their host galaxy centres for a sample of SNe IIb.

Hereafter, by the distance between a supernova and its host galaxy we mean the projection of the distance onto the picture plane, which is obviously smaller than the real distance. However, the star-evolution theory predicts that CCSNe including SNe IIb mainly appear in the galactic planes of spiral galaxies, in regions of high star-formation rate. Therefore, we assume that the contribution of the projection onto the line of sight is relatively small and this underestimation of the distance does not significantly affect our analysis.

We collected 71 confirmed SNe IIb and 108 candidates for SNe IIb from the Open Supernova Catalog (Guillochon et al. 2017). The confirmed SNe IIb are supernovae for which multiple spectra have been obtained and a detailed spectral analysis has been performed. If only a spectrum is available (usually single spectroscopic confirmation following the astronomical telegram about the transient discovery) we consider a supernova as a SN IIb candidate.

First, we calculated the absolute galactocentric distance D for each object as $D \approx d_a \times \Theta$. The angle Θ is the angle between the supernova and the host galaxy centre. The angular distance d_a for flat Λ CDM cosmology with $\Omega_{\Lambda} = 0.7$ and $H_0 = 70 \text{ km s}^{-1} \text{ Mpc}^{-1}$ is

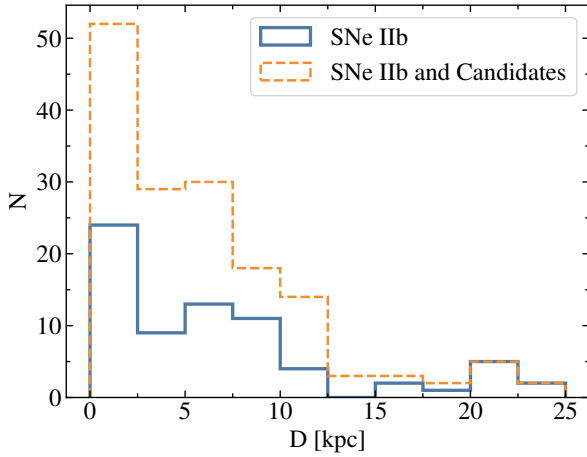
$$d_a = \frac{c}{H_0 \times (1+z)} \int_0^z \frac{dz'}{\sqrt{(1-\Omega_{\Lambda}) \times (1+z')^3 + \Omega_{\Lambda}}}, \quad (3)$$

where z is the redshift and c is the speed of light. The distribution of Type IIb Supernovae by D is presented in Fig. 10. Most SNe IIb, about 85 per cent, are located inside a radius of 12 kpc. However, there is a local maximum near 20 kpc, which may be due to the fact that the radius of galaxies can vary widely.

To perform a more accurate analysis we determined the SN-host separation relative to the host size. To characterise the size of a galaxy we used a D_{25} value, which is the major diameter measured to the *B*-passband 25 mag arcsec $^{-2}$ isophote. The D_{25} values were

Table 5. Comparison of the hydrodynamic modelling results for different SNe I Ib.

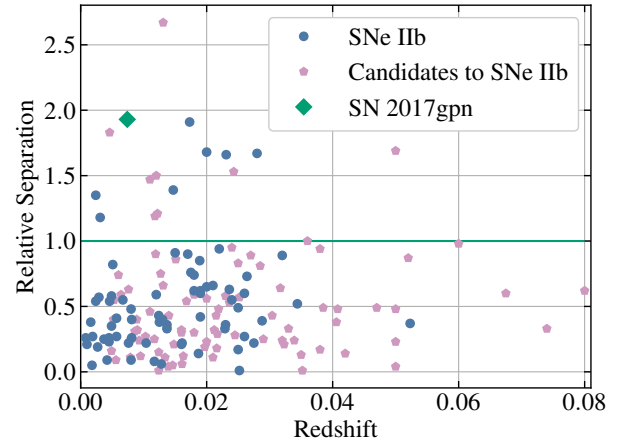
SN name	M_{CR} [M_{\odot}]	M_{ej} [M_{\odot}]	$M_{56\text{Ni}}$ [M_{\odot}]	$M_{\text{H,env}}$ [M_{\odot}]	R [R_{\odot}]	E_{exp} [10^{51} erg]	Reference
1993J	~ 1.4	1.4–3.1	0.06–0.08	0.2	430–720	1.2	Woosley et al. (1994) Blinnikov et al. (1998)
2008ax	1.41	2.39	0.11	–	600	1.5	Tsvetkov et al. (2009)
2008ax	1.5	1.8–3.5	0.05–0.07	0.06	30–50	0.8–1.2	Folatelli et al. (2015)
2011hs	1.5	1.5–2.5	0.04	<0.5	500–600	0.85	Bufano et al. (2014)
2011fu	1.5	3.5	0.15	0.3	450	1.3	Morales-Garoffolo et al. (2015)
2011dh	1.41	2.24–4.24	0.07	–	150–300	2–4	Tsvetkov et al. (2012)
2011dh	1.5	2	0.06	0.1	200	0.6–1	Bersten et al. (2012)
2016gkg	1.4	3.55	0.2	0.02	180–260	1.3	Piro et al. (2017)
2016gkg	1.5–1.6	2.5–3.4	0.085–0.087	0.01–0.09	300–340	1–1.2	Bersten et al. (2018)

**Figure 10.** Histogram of the supernovae distribution depending on the projection of the distance between SN and its host galaxy centre, D . The orange dashed line corresponds to all considered supernovae including confirmed SNe I Ib and candidates for SNe I Ib. The solid blue line corresponds to the distribution of confirmed SNe I Ib only.

extracted from the HyperLEDA extragalactic data base (Makarov et al. 2014).

The full list of studied supernovae and the absolute and relative distances are summarised in Table A1: the first column is the number in the list for easier searching, the second column consists of the supernova names starting with confirmed SNe I Ib, and continuing with SNe I Ib candidates. The equatorial coordinates (RA, Dec.) of supernovae and their host galaxies are presented in the third, fourth, fifth and sixth columns, respectively. The seventh column indicates the redshift z . D_{25} is given in column eight. The angle Θ expressed in arcsec is shown in the ninth column. Columns 10 and 11 contain the absolute distance D in kpc and relative separation normalized to the size of the host galaxies, respectively.

In Fig. 11 we present the relative separation between SNe and their host galaxies depending on the redshift. To evaluate how far away a supernova is, we chose a value of 1 for the relative separation, which is shown by the horizontal green line in Fig. 11. There are eight SNe I Ib that lie above the solid green line; we collect them

**Figure 11.** Relative separation between supernovae and their host galaxy centres as a function of redshift. Confirmed SNe I Ib are plotted in blue dots; candidates for SNe I Ib, in pink pentagons; and the studied SN 2017gpn is marked with the green diamond. SNe above the green line are considered to be distant from the centres of their hosts.

into a group of distant supernovae. SN 2017gpn is the most distant from the host galaxy centre among the confirmed SNe I Ib.

After that, we collected images for all these distant SNe with the goal of investigating their unexpected location (see Fig. 12). The majority of them are in continuations of spiral arms, e.g. supernovae 1997dd or 2001cf. Exceptions are supernovae 2011ft and 2017gpn, which are well outside the borders of their host galaxies. We found Pan-STARRS1 images (Chambers et al. 2016; Flewelling et al. 2016) for SN 2011ft in the r , i , z and y passbands where one can notice a diffuse red object exactly at the SN 2011ft position, which can be associated with the host galaxy of SN 2011ft.

In addition, we consider the object with the highest relative separation in Fig. 11 (rel. sep. is 2.67; see Table A1), SN 2017ati, a candidate for type I Ib SNe. It turns out that this SN exploded in a system of interacting galaxies. Due to this interaction, a region with a high star-formation rate could be formed, and this explains the detection of the core-collapse supernova far from the host galaxy disc. Therefore, SN 2017gpn is the only distant SNe that is not located in a region with a high star-formation rate.

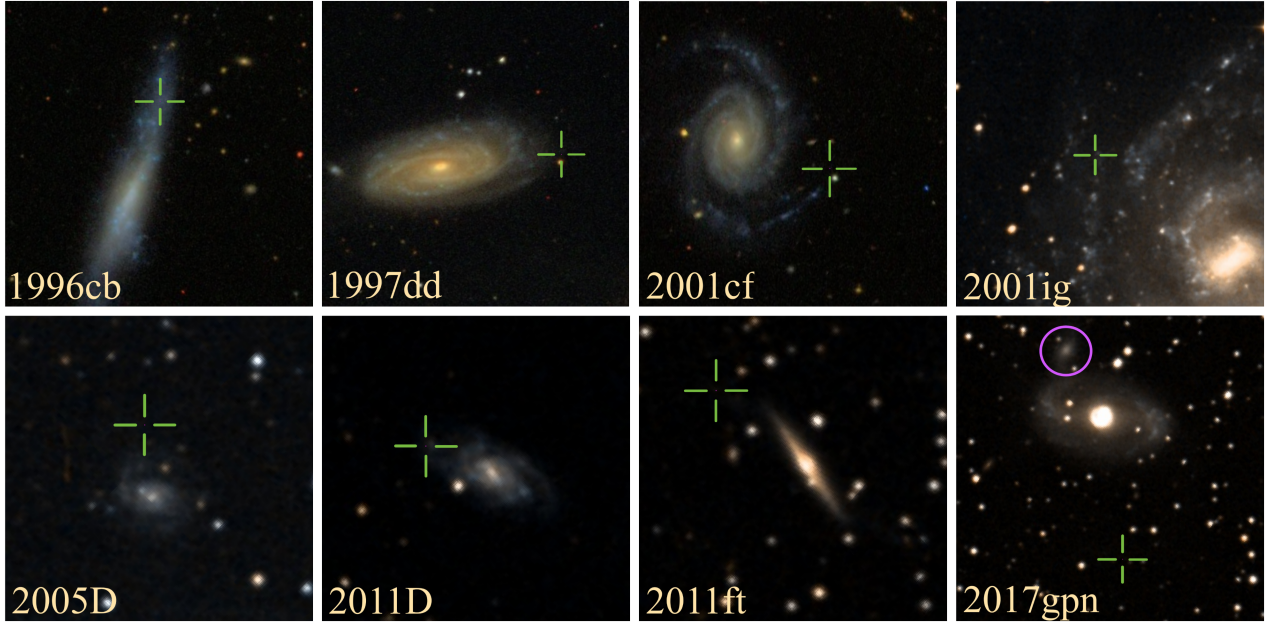


Figure 12. Optical images of supernovae distant from their host galaxy centres. SNe are marked by green crosses. All images were provided by SDSS (Blanton et al. 2017; Gunn et al. 1998) and DSS. The purple circle denotes the galaxy ZOAG G134.74+13.65.

According to the stellar evolution theory, the progenitor star of SN IIb should be a massive star with an initial mass of $\sim 30 M_{\odot}$. The fact that SN 2017gpn exploded far from a region with a high star-formation rate challenges this popular scenario. We have considered three different hypotheses to explain its location.

First, the progenitor of SN 2017gpn could be a superspeed star. Brown et al. (2005) have discovered a hypervelocity star SDSS J090745.0+024507 with a mass of $\sim 4 M_{\odot}$ ejected from the Milky Way centre and left with a velocity of 709 km s^{-1} . If we presume that the SN 2017gpn progenitor mass is about $30 M_{\odot}$, the average lifetime of such a star will be $\sim 3 \text{ Myr}$ calculated by the formula $t_{\text{life}} \simeq \left(\frac{M_{\odot}}{M_{\text{star}}} \right)^2$. If it moves at a speed of 1000 km s^{-1} (Hills 1988), it could move away from the centre of the host galaxy by $\sim 29 \text{ kpc}$ during its lifetime. However, such a high velocity implies that the kinetic energy is $\sim 3 \times 10^{50} \text{ erg}$; therefore an effective mechanism of star acceleration is required.

The second hypothesis is that part of the spiral arm of the host galaxy NGC 1343 is faint and therefore cannot be easily observed. For example, a similar situation is observed for the object AM 1316–241 (Keel & White 2001; see Fig. 13). In this case we can see the faint spiral arm of the galaxy only because it is illuminated by the light of a background elliptical galaxy. It is important that this part of the spiral structure does not lie on the continuation of the bright spiral arm; therefore, a SN explosion there (in the absence of a “lamp” behind) will appear to be outside the galaxy.

The third hypothesis is that the host galaxy of SN 2017gpn experienced an interaction with other galaxies in the past. Tidal force destroyed the satellite galaxy and provided enough gas, which could condense far from the NGC 1343 centre. Moreover, we can see the interaction between the galaxy ZOAG G134.74+13.65 and the SN 2017gpn host galaxy, which could also cause the formation of gas clouds with a high star-formation rate (see Fig. 12, panel 8).

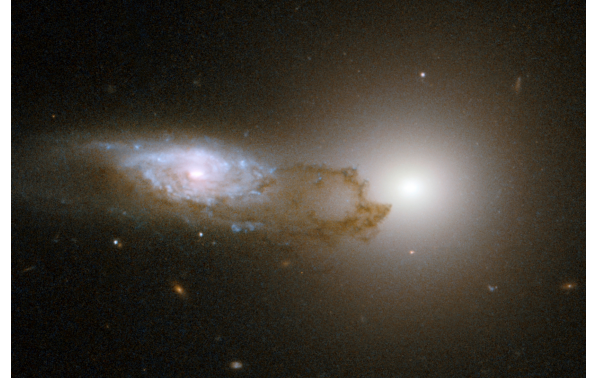


Figure 13. An image of AM 1316–241 obtained by the Hubble Space Telescope (Keel & White 2001). The faint spiral arms are visible owing to the light from the background elliptical galaxy.

4.5 Connection with G299232

Initially SN 2017gpn was considered as a possible optical counterpart of the GW event G299232 since it was discovered 2 d later in its error-box⁴. If we assume that gravitational energy is released by a collapse, GW events are expected from supernova explosions (Herant et al. 1994) and could be detected by the LIGO/Virgo experiment (The LIGO Scientific Collaboration et al. 2019).

Nevertheless, the results of the hydrodynamic modelling show that the explosion happened on Aug 20 ($\sim 3.5 \text{ d}$ before the GW alert) following the best-fitting model, or on Aug 17 for the additional model, i.e. $\sim 8 \text{ d}$ before registration of G299232. G299232 is a low-significance event, so it could be a false signal; even if it is not, it is still implausible that SN 2017gpn could be associated with this

⁴ <https://gcn.gsfc.nasa.gov/other/G299232.gcn3>

alert. Neither of our calculated models favor the electromagnetic counterpart of the gravitational event.

5 CONCLUSIONS

In this paper we have presented spectroscopic and photometric observations of the Type IIb Supernova 2017gpn and the results of the numerical modelling of its *B*, *R* light curves with the STELLA code. The best-fitting hydrodynamic model has the following parameter values: pre-SN radius $50 R_{\odot}$, pre-SN mass $3.5 M_{\odot}$, mass of synthesized nickel totally mixed in the envelope $0.11 M_{\odot}$, mass of the compact remnant $1.41 M_{\odot}$ (i.e. neutron star as a remnant), and energy of the explosion 1.2×10^{51} erg. We also determined the ranges for these parameters by considering the dependence of the modelled light curves on each parameter while the others remain fixed. The obtained ranges are $3\text{--}4 M_{\odot}$ for the pre-SN mass, $20\text{--}70 R_{\odot}$ for the pre-SN radius, $0.09\text{--}0.13 M_{\odot}$ for the mass of ^{56}Ni , and, finally, $(1.05\text{--}1.60) \times 10^{51}$ erg for E_{exp} .

The study of Type IIb Supernovae is an important part of the exploration of the chemical composition of the Universe. The nucleosynthesis yields of CCSNe including SNe IIb are characterized by strong contributions to the so-called alpha elements O, Ne, Mg, Si, S, Ar, Ca, and Ti (Thielemann et al. 2018) and the heavy elements, namely Ni, Co and Fe.

According to the Open Supernova Catalog (Guillochon et al. 2017) only about a couple of dozen SNe IIb have detailed photometry that allows the performance of reliable hydrodynamic modelling. Some of these SNe are considered in this paper and compared with SN 2017gpn taking into account a physically motivated classification of stripped-envelope SNe proposed by Prentice & Mazzali (2017). In this classification SN 2017gpn belongs to the group IIb(I) which is characterized by strong hydrogen line profiles before maximum light, which weaken greatly over time, and $H\alpha$ P Cygni profile dominated by the absorption component. Analysis of the hydrodynamic modelling results of different SNe IIb shows that the mass of synthesised ^{56}Ni is in the range $0.05\text{--}0.15 M_{\odot}$.

The modelling results for SN 2017gpn are consistent with those for SNe IIb considered, especially if we compare them with the modelling results for SN 2008ax which is of IIb(I) group according to Prentice & Mazzali (2017). These results together with the observational data presented here contribute to the study of the Type IIb SN phenomenon, increasing the sample of well-studied SNe IIb.

Finally, we considered three different hypotheses that could explain SN 2017gpn's distant location relative to its host galaxy:

- the progenitor of SN 2017gpn is a hypervelocity star ejected by NGC 1343 with an average speed more than 1000 km s^{-1} ;
- the progenitor exploded in a faint spiral arm of the host galaxy;
- the progenitor is formed in a region of interaction between the host galaxy and another galaxy in the past.

However, there is still a chance that the SN 2017gpn progenitor was not a massive star exploding for some reason far from regions of high star-formation rate. A similar idea was proposed for the Type Ibn Supernova PS1-12sk by Hosseinzadeh et al. (2019). This question is open and challenges modern star-evolution models.

ACKNOWLEDGEMENTS

EAB acknowledges support from a Russian Science Foundation grant 18-72-00159 for studying the question of the distant posi-

tion of SN 2017gpn relative host galaxy centre. SIB and MVP acknowledge support from a Russian Science Foundation grant 18-12-00522 for supernova modelling with the STELLA code. The authors acknowledge the support from the Program of Development of M.V. Lomonosov Moscow State University (Leading Scientific School “Physics of stars, relativistic objects and galaxies”). The authors are grateful to O. I. Spiridonova and the Zeiss-1000 staff for help with observations. We thank K. L. Malanchev and M. Sh. Potashov for helpful discussions. XW is supported by the National Natural Science Foundation of China (NSFC grants 11325313, 11633002, and 11761141001), and the National Program on Key Research and Development Project (grant no. 2016YFA0400803). We acknowledge the support of the staff of the Xinglong 2.16-m telescope. This work was partially supported by the Open Project Program of the Key Laboratory of Optical Astronomy, National Astronomical Observatories, Chinese Academy of Sciences. This research has made use of NASA's Astrophysics Data System Bibliographic Services and the following PYTHON software packages: NUMPY (van der Walt et al. 2011), MATPLOTLIB (Hunter 2007), ASTROPY (Astropy Collaboration et al. 2013; Price-Whelan et al. 2018).

6 DATA AVAILABILITY

The data underlying this article are available in the article.

REFERENCES

- Anderson J. P., et al., 2014, *ApJ*, **786**, 67
 Arnett W. D., 1982, *ApJ*, **253**, 785
 Astropy Collaboration et al., 2013, *A&A*, **558**, A33
 Audcent-Ross F. M., Meurer G. R., Audcent J. R., Ryder S. D., Wong O. I., Phan J., Williamson A., Kim J. H., 2020, *MNRAS*, **492**, 848
 Baklanov P. V., Blinnikov S. I., Pavlyuk N. N., 2005, *Astronomy Letters*, **31**, 429
 Barbon R., Benetti S., Cappellaro E., Patat F., Turatto M., Iijima T., 1995, *A&AS*, **110**, 513
 Bersten M. C., et al., 2012, *ApJ*, **757**, 31
 Bersten M. C., et al., 2018, *Nature*, **554**, 497
 Blanton M. R., et al., 2017, *AJ*, **154**, 28
 Blinnikov S. I., Bartunov O. S., 1993, *A&A*, **273**, 106
 Blinnikov S. I., Eastman R., Bartunov O. S., Popolitov V. A., Woosley S. E., 1998, *ApJ*, **496**, 454
 Blinnikov S. I., Röpke F. K., Sorokina E. I., Gieseler M., Reinecke M., Travaglio C., Hillebrandt W., Stritzinger M., 2006, *A&A*, **453**, 229
 Blondin S., Tonry J. L., 2007, *ApJ*, **666**, 1024
 Branch D., 1992, *ApJ*, **392**, 35
 Brown W. R., Geller M. J., Kenyon S. J., Kurtz M. J., 2005, *ApJ*, **622**, L33
 Bufano F., et al., 2014, *MNRAS*, **439**, 1807
 Caimmi M., 2017, Transient Name Server Discovery Report, **2017-973**, 1
 Chambers K. C., et al., 2016, arXiv e-prints,
 Chugai N. N., et al., 2004, *MNRAS*, **352**, 1213
 Clocchiatti A., Wheeler J. C., 1997, *ApJ*, **491**, 375
 Copperwheat C. M., et al., 2017, GRB Coordinates Network, **21755**, 1
 Dessart L., Hillier D. J., 2005, *A&A*, **439**, 671
 Dessart L., Hillier D. J., 2006, *A&A*, **447**, 691
 Filippenko A. V., 1997, *ARA&A*, **35**, 309
 Filippenko A. V., Matheson T., Ho L. C., 1993, *ApJ*, **415**, L103
 Flewelling H. A., et al., 2016, arXiv e-prints,
 Folatelli G., et al., 2006, *ApJ*, **641**, 1039
 Folatelli G., Bersten M. C., Kuncarayakti H., Benvenuto O. G., Maeda K., Nomoto K., 2015, *ApJ*, **811**, 147
 Guillochon J., Parrent J., Kelley L. Z., Margutti R., 2017, *ApJ*, **835**, 64
 Gunn J. E., et al., 1998, *AJ*, **116**, 3040

- Hakobyan A. A., Adibekyan V. Z., Aramyan L. S., Petrosian A. R., Gomes J. M., Mamon G. A., Kunth D., Turatto M., 2012, *A&A*, **544**, A81
- Hakobyan A. A., et al., 2016, *MNRAS*, **456**, 2848
- Herant M., Benz W., Hix W. R., Fryer C. L., Colgate S. A., 1994, *ApJ*, **435**, 339
- Hills J. G., 1988, *Nature*, **331**, 687
- Hoflich P., Langer N., Duschinger M., 1993, *A&A*, **275**, L29
- Holmes S., et al., 2011, *Publications of the Astronomical Society of the Pacific*, **123**, 1177
- Hosseinzadeh G., McCully C., Zabludoff A. I., Arcavi I., French K. D., Howell D. A., Berger E., Hiramatsu D., 2019, *ApJ*, **871**, L9
- Hunter J. D., 2007, *Computing in Science and Engineering*, **9**, 90
- Imshennik V. S., Nadezhin D. K., 1983, *Soviet Scientific Reviews, Section E: Astrophysics and Space Physics Reviews*, **2**, 75
- Jonker P. G., Fraser M., Nissanke S., Fender R. P., Broderick J., Rowlinson A., Wijers R. A. M. J., Stappers B., 2017, *GRB Coordinates Network*, **21737**, 1
- Kasen D., Branch D., Baron E., Jeffery D., 2002, *ApJ*, **565**, 380
- Keel W. C., White R. E., 2001, *ApJ*, **121**, 1442
- Komarov V. V., Komarova V. N., Moskvitin A. S., Drabek S. V., Emelyanov E. V., Shergin V. S., 2020, *Astronomical Journal of Azerbaijan*, p. in press
- Kozyreva A., et al., 2017, *MNRAS*, **464**, 2854
- Kromer M., Sim S. A., 2009, *MNRAS*, **398**, 1809
- Kumar B., et al., 2013, *MNRAS*, **431**, 308
- Landolt A. U., 1992, *AJ*, **104**, 340
- Lipunov V., et al., 2010, *Advances in Astronomy*, **2010**, 349171
- Lipunov V. M., et al., 2017, *GRB Coordinates Network*, **21719**, 1
- Makarov D., Prugniel P., Terekhova N., Courtois H., Vauglin I., 2014, *A&A*, **570**, A13
- Modjaz M., et al., 2014, *AJ*, **147**, 99
- Morales-Garoffolo A., et al., 2015, *MNRAS*, **454**, 95
- Nadyozhin D. K., Razinkova T. L., 1986, *Nauchnye Informatsii*, **61**, 29
- Nicholl M., 2018, *Research Notes of the AAS*, **2**, 230
- Nomoto K., Suzuki T., Shigeyama T., Kumagai S., Yamaoka H., Saio H., 1993, *Nature*, **364**, 507
- Paxton B., et al., 2018, *ApJS*, **234**, 34
- Pessi P. J., et al., 2019, *MNRAS*, **488**, 4239
- Piro A. L., Muhleisen M., Arcavi I., Sand D. J., Tartaglia L., Valenti S., 2017, *ApJ*, **846**, 94
- Prentice S. J., Mazzali P. A., 2017, *MNRAS*, **469**, 2672
- Price-Whelan A. M., et al., 2018, *AJ*, **156**, 123
- Qiu Y., Li W., Qiao Q., Hu J., 1999, *AJ*, **117**, 736
- Richmond M. W., Treffers R. R., Filippenko A. V., Paik Y., 1996, *AJ*, **112**, 732
- Roberts D., Kolb U., 2018, **2**
- Rui L., et al., 2017, *The Astronomer's Telegram*, **10681**
- Sanders N. E., et al., 2015, *The Astrophysical Journal*, **799**, 208
- Schlaflly E. F., Finkbeiner D. P., 2011, *ApJ*, **737**, 103
- Sim S. A., Kromer M., Röpke F. K., Sorokina E. I., Blinnikov S. I., Kasen D., Hillebrandt W., 2010, in Pogorelov N. V., Audit E., Zank G. P., eds, *Astronomical Society of the Pacific Conference Series Vol. 429, Numerical Modeling of Space Plasma Flows*, Astronom-2009. p. 148 ([arXiv:0911.1549](https://arxiv.org/abs/0911.1549))
- Sobolev V. V., 1960, *Moving envelopes of stars*
- Springob C. M., Haynes M. P., Giovanelli R., Kent B. R., 2005, *ApJS*, **160**, 149
- Stetson P. B., 1987, in *Bulletin of the American Astronomical Society*. p. 745
- Tauris T. M., Langer N., Moriya T. J., Podsiadlowski P., Yoon S.-C., Blinnikov S. I., 2013, *ApJ*, **778**, L23
- The LIGO Scientific Collaboration et al., 2019, *arXiv e-prints*, p. [arXiv:1908.03584](https://arxiv.org/abs/1908.03584)
- Thielemann F.-K., Isern J., Perego A., von Ballmoos P., 2018, *Space Sci. Rev.*, **214**, 62
- Tominaga N., Blinnikov S., Baklanov P., Morokuma T., Nomoto K., Suzuki T., 2009, *ApJ*, **705**, L10
- Tsang B. T. H., Goldberg J. A., Bildsten L., Kasen D., 2020, *arXiv e-prints*, p. [arXiv:2006.01832](https://arxiv.org/abs/2006.01832)
- Tsvetkov D. Y., Volkov I. M., Baklanov P., Blinnikov S., Tuchin O., 2009, *Peremennye Zvezdy*, **29**
- Tsvetkov D. Y., Volkov I. M., Sorokina E., Blinnikov S., Pavlyuk N., Borisov G., 2012, *Peremennye Zvezdy*, **32**
- Volnova A. A., et al., 2017, *MNRAS*, **467**, 3500
- Wang X., 2017, *The Astronomer's Telegram*, **10684**, 1
- Woosley S. E., Eastman R. G., Weaver T. A., Pinto P. A., 1994, *ApJ*, **429**, 300
- Woosley S. E., Kasen D., Blinnikov S., Sorokina E., 2007, *ApJ*, **662**, 487
- Yoon S.-C., Dessart L., Clocchiatti A., 2017, *ApJ*, **840**, 10
- van der Walt S., Colbert S. C., Varoquaux G., 2011, *Computing in Science and Engineering*, **13**, 22

APPENDIX A: TABLE

Table A1: A complete list of confirmed Type IIb Supernovae and candidates to SNe IIb.

Nº	SN name	R.A. _{SN}	Dec. _{SN}	R.A. _{Host}	Dec. _{Host}	z	D ₂₅ ["]	Θ ["]	D [kpc]	Rel. Sep.
1	SN1987K	12 43 41.17	+16 23 44.9	12 43 42.63	+16 23 36.2	0.0027	233.43	22.74	1.27	0.19
2	SN1993J	09 55 24.77	+69 01 13.7	09 55 33.17	+69 03 55.1	0.0008	1312.66	167.57	2.78	0.26
3	SN1996cb	11 03 41.98	+28 54 13.7	11 03 43.41	+28 53 13.9	0.0024	92.93	62.68	3.11	1.35
4	SN1997dd	16 05 46.33	+21 29 14.2	16 05 51.98	+21 29 05.9	0.0147	114.33	79.30	23.77	1.39
5	SN1998fa	06 42 51.51	+41 25 18.9	06 42 51.76	+41 25 14.9	0.0250	57.3	4.89	2.46	0.17
6	SN2000H	06 51 07.67	+12 55 18.5	06 51 06.28	+12 55 19.4	0.0130	101.89	20.34	5.40	0.40
7	SN2001ef	12 02 31.64	+41 02 58.9	12 02 36.56	+41 03 15.0	0.0200	68.89	57.94	23.48	1.68
8	SN2001gd	13 13 23.89	+36 38 17.7	13 13 27.54	+36 35 37.1	0.0029	586.34	166.50	9.99	0.57
9	SN2001ig	22 57 30.69	-41 02 25.9	22 57 18.36	-41 04 14.5	0.0031	300.71	176.76	11.33	1.18
10	SN2001IQ	11 25 19.77	+63 43 15.6	11 25 19.05	+63 43 45.4	0.0124	140.65	30.18	7.65	0.43
11	SN2002au	09 34 37.60	+05 50 15.7	09 34 38.62	+05 50 29.2	0.0180	65.79	20.34	7.44	0.62
12	SN2002eg	19 49 47.25	+50 41 53.6	19 49 48.75	+50 41 46.0	0.0260	53.48	16.15	8.45	0.60
13	SN2003bg	04 10 59.43	-31 24 50.4	04 11 00.65	-31 24 27.8	0.0046	101.89	27.47	2.61	0.54
14	SN2003cv	11 17 48.30	+19 09 08.5	11 17 48.37	+19 09 05.4	0.0288	16.53	3.25	1.88	0.39
15	SN2003ed	13 47 45.40	+38 18 21.1	13 47 44.99	+38 18 16.4	0.0045	52.26	6.74	0.63	0.26
16	SN2003gu	23 02 59.45	+34 43 19.6	23 02 59.10	+34 43 37.7	0.0190	60.00	18.61	7.17	0.62
17	SN2003ki	07 51 33.24	+63 55 51.6	07 51 34.20	+63 55 42.0	0.0250	46.57	11.50	5.79	0.49
18	SN2004be	10 00 19.47	-24 48 13.8	10 00 19.30	-24 48 08.0	0.0076	56.00	6.24	0.98	0.22
19	SN2004bi	10 47 37.45	+26 18 12.0	10 47 39.37	+26 17 41.5	0.0220	84.75	39.96	17.77	0.94
20	SN2004bm	10 52 35.33	+22 56 05.5	10 52 35.75	+22 56 02.8	0.0042	140.65	6.40	0.56	0.09
21	SN2004c	11 27 29.76	+56 52 48.4	11 27 31.89	+56 52 36.2	0.0057	104.27	21.30	2.50	0.41
22	SN2004ex	00 38 10.19	+02 43 17.2	00 38 12.38	+02 43 42.6	0.0180	111.73	41.50	15.17	0.74
23	SN2004ff	04 58 46.19	-21 34 12.0	04 58 47.12	-21 34 09.9	0.0230	73.82	13.14	6.10	0.36
24	SN2004gj	11 30 59.63	+20 28 06.8	11 31 00.66	+20 28 08.6	0.0210	44.48	14.59	6.20	0.66
25	SN2005D	07 26 57.36	+20 22 53.4	07 26 57.12	+20 22 15.5	0.0280	45.51	38.05	21.38	1.67
26	SN2005em	03 13 47.71	-00 14 37.0	03 13 47.69	-00 14 36.7	0.0252	95.09	0.42	0.22	0.01
27	SN2005H	02 09 38.52	-10 08 43.6	02 09 38.56	-10 08 46.1	0.0128	80.94	2.57	0.67	0.06
28	SN2005U	11 28 33.22	+58 33 42.5	11 28 31.33	+58 33 41.8	0.0010	143.93	14.80	0.31	0.21
29	SN2006ba	09 43 13.40	-09 36 53.0	09 43 11.98	-09 36 44.5	0.0190	106.70	22.66	8.73	0.42
30	SN2006bf	12 58 50.68	+09 39 30.1	12 58 50.91	+09 39 14.7	0.0240	57.30	15.77	7.63	0.55
31	SN2006el	22 47 38.50	+39 52 27.6	22 47 37.39	+39 52 44.8	0.0170	47.66	21.43	7.41	0.90
32	SN2006iv	11 48 12.35	+54 59 14.6	11 48 11.32	+54 59 30.2	0.0081	88.75	17.94	2.99	0.40
33	SN2006qp	14 42 30.65	+28 43 25.9	14 42 33.24	+28 43 35.2	0.0120	119.72	35.32	8.67	0.59
34	SN2006T	09 54 30.21	-25 42 29.3	09 54 28.64	-25 42 11.8	0.0081	212.89	27.50	4.58	0.26
35	SN2007ay	08 17 14.85	+01 12 06.9	08 17 15.73	+01 12 23.0	0.0150	45.51	20.82	6.37	0.91
36	SN2008aq	12 50 30.42	-10 52 01.4	12 50 29.39	-10 51 15.7	0.0080	198.68	48.15	7.92	0.48
37	SN2008ax	12 30 40.80	+41 38 14.5	12 30 36.41	+41 38 37.4	0.0019	405.65	54.28	2.14	0.27
38	SN2008ay	12 55 26.36	+52 16 15.5	12 55 24.90	+52 16 03.5	0.0344	68.89	17.99	12.32	0.52
39	SN2008bo	18 19 54.34	+74 34 20.9	18 19 46.42	+74 34 06.2	0.0049	198.68	34.86	3.53	0.35
40	SN2008cx	00 56 45.90	-09 54 19.0	00 56 42.66	-09 54 50.1	0.0189	134.32	57.09	21.89	0.85
41	SN2008ie	02 43 20.80	+04 58 19.1	02 43 22.27	+04 58 06.2	0.0137	140.65	25.47	7.13	0.36
42	SN2009C	23 13 42.84	+49 40 47.2	23 13 43.95	+49 40 35.7	0.0236	49.91	15.76	7.50	0.63

43	SN2009gk	21 44 27.28	+14 53 57.3	21 44 28.76	+14 53 59.2	0.0264	58.63	21.54	11.43	0.73
44	SN2009jv	09 40 57.83	+47 37 04.0	09 40 58.19	+47 37 13.3	0.0161	90.81	9.99	3.27	0.22
45	SN2009K	04 36 36.77	-00 08 35.6	04 36 37.35	-00 08 37.0	0.0117	208.04	8.81	2.11	0.08
46	SN2009mk	00 06 21.37	-41 28 59.8	00 06 19.92	-41 29 59.6	0.0051	150.71	61.98	6.52	0.82
47	SN2010am	09 33 01.75	+15 49 08.8	09 33 02.11	+15 49 16.1	0.0200	27.20*	8.96	3.63	0.65
48	SN2010cn	11 04 06.57	+04 49 58.7	11 04 06.40	+04 49 55.5	0.0260	30.30*	4.09	2.14	0.27
49	SN2010ei	14 54 07.69	+42 32 54.6	14 54 07.71	+42 32 53.2	0.0187	20.20*	1.42	0.54	0.14
50	SN2010ej	14 13 56.74	+31 32 25.1	14 13 56.56	+31 32 24.7	0.0523	12.54	2.34	2.38	0.37
51	SN2010ek	22 48 40.96	+27 37 11.4	22 48 40.80	+27 36 40.0	0.0320	70.49	31.47	20.12	0.89
52	SN2011bp	11 12 29.96	+31 23 05.5	11 12 30.16	+31 23 05.9	0.0275	23.89	2.59	1.43	0.22
53	SN2011D	03 02 14.53	+17 20 58.3	03 02 12.23	+17 20 43.7	0.0231	43.47	36.02	16.80	1.66
54	SN2011dh	13 30 05.11	+47 10 10.9	13 29 52.70	+47 11 43.0	0.0016	828.23	156.49	5.19	0.38
55	SN2011ft	17 52 42.98	+29 04 10.6	17 52 39.46	+29 03 32.4	0.0173	62.83	59.91	21.07	1.91
56	SN2011fu	02 08 21.40	+41 29 12.3	02 08 21.49	+41 28 45.1	0.0190	90.81	27.22	10.49	0.60
57	SN2011hs	22 57 11.77	-43 23 04.8	22 57 13.57	-43 23 46.1	0.0057	337.40	45.72	5.37	0.27
58	SN2012P	14 59 59.04	+01 53 24.4	15 00 00.43	+01 53 28.6	0.0045	181.20	21.26	1.98	0.23
59	SN2013ak	08 07 06.69	-28 03 10.1	08 07 08.00	-28 03 08.0	0.0037	140.65	17.47	1.34	0.25
60	SN2013bb	14 12 13.96	+15 50 31.5	14 12 15.81	+15 50 30.9	0.0175	70.49	26.70	9.50	0.76
61	SN2013df	12 26 29.33	+31 13 38.3	12 26 27.09	+31 13 24.8	0.0024	116.99	31.75	1.58	0.54
62	SN2014ds	08 11 16.45	+25 10 47.4	08 11 15.92	+25 10 45.7	0.0137	44.48	7.39	2.07	0.33
63	SN2015bi	14 32 15.31	+26 19 32.0	14 32 15.19	+26 19 36.2	0.0160	42.48	4.50	1.47	0.21
64	SN2016adj	13 25 24.12	-43 00 57.9	13 25 27.60	-43 01 08.8	0.0018	1542.24	39.69	1.48	0.05
65	SN2016gkg	01 34 14.46	-29 26 25.0	01 34 18.24	-29 25 06.6	0.0049	322.22	92.66	9.37	0.58
66	SN2017gpn	03 37 44.97	+72 31 59.0	03 37 49.72	+72 34 16.6	0.0074	143.93	139.25	21.20	1.93
67	ASASSN-14az	23 44 48.00	-02 07 03.2	23 44 48.27	-02 06 53.4	0.0067	38.74	10.6	1.46	0.55
68	ASASSN-14dq	21 57 59.97	+24 16 08.1	21 57 59.82	+24 15 59.7	0.0104	79.10	8.65	1.84	0.22
69	ASASSN-15bd	15 54 38.33	+16 36 38.9	15 54 38.39	+16 36 37.6	0.0080	22.81	1.00	0.16	0.09
70	PS15cjr	02 38 07.29	+01 23 29.2	02 38 07.57	+01 23 18.1	0.0229	72.14	11.87	5.49	0.33
71	PTF11iqb	00 34 04.84	-09 42 17.9	00 34 02.79	-09 42 19.0	0.0125	157.82	30.33	7.75	0.38
72	SN2001ad*	17 24 02.40	+58 59 52.0	17 24 08.11	+58 59 42.4	0.0110	61.40	45.15	10.17	1.47
73	SN2002hz*	22 27 49.54	+38 35 09.5	22 27 48.30	+38 35 11.7	0.0180	99.58	14.70	5.38	0.30
74	SN2002jz*	04 13 12.52	+13 25 07.3	04 13 12.40	+13 25 19.1	0.0052	60.00	11.93	1.28	0.40
75	SN2005by*	13 45 46.91	+22 05 46.8	13 45 45.62	+22 05 18.4	0.0270	75.54	33.59	18.22	0.89
76	SN2005lr*	07 11 39.03	-26 42 20.2	07 11 40.45	-26 42 17.9	0.0086	125.36	19.17	3.39	0.31
77	SN2006ss*	14 20 27.46	+35 11 42.7	14 20 26.50	+35 11 19.1	0.0120	88.75	26.37	6.48	0.59
78	SN2008cw*	16 32 38.27	+41 27 33.2	16 32 38.00	+41 27 33.0	0.0320	25.59	3.04	1.94	0.24
79	SN2008gx*	10 15 32.95	+74 12 59.1	10 15 32.22	+74 13 13.1	0.0215	67.32	14.31	6.22	0.43
80	SN2009gj*	00 30 28.56	-33 12 56.0	00 30 21.89	-33 14 43.3	0.0053	499.06	136.08	14.88	0.55
81	SN2009mg*	06 21 44.86	-59 44 26.0	06 21 38.91	-59 44 24.0	0.0076	143.93	45.02	7.04	0.63
82	SN2009Z*	14 01 53.61	-01 20 30.2	14 01 53.80	-01 20 35.6					
83	SN2010jr*	05 19 35.80	-32 39 28.2	05 19 35.81	-32 39 27.9	0.0124	82.82	0.33	0.08	0.01
84	SN2011bv*	13 02 53.57	-04 02 36.0							
85	SN2011cb*	22 47 07.49	-64 49 43.4	22 47 06.26	-64 49 55.4	0.0079	261.91	14.34	2.33	0.11
86	SN2011ef*	23 30 57.02	+15 29 24.3	23 30 56.80	+15 29 26.0	0.0134	64.29	3.61	0.99	0.11
87	SN2011ei*	20 34 22.62	-31 58 23.6	20 34 21.00	-31 58 51.0	0.0093	280.64	34.29	6.55	0.24
88	SN2011hg*	23 11 48.84	+31 01 00.4	23 11 50.29	+31 01 16.2	0.0236	92.93	24.44	11.64	0.53

89	SN2012cd*	13 22 35.25	+54 48 47.0	13 22 32.43	+54 49 05.0	0.0118	51.07	30.30	7.32	1.19
90	SN2012dy*	21 18 50.70	-57 38 42.5	21 18 50.99	-57 38 25.2	0.0103	128.28	17.46	3.69	0.27
91	SN2012fg*	09 24 37.95	+49 21 32.0	09 24 37.73	+49 21 25.5	0.0163	114.33	6.85	2.27	0.12
92	SN2012hb*	09 02 05.46	-64 54 19.7	09 02 05.52	-64 54 16.2	0.0056	80.94	3.52	0.41	0.09
93	SN2012hs*	09 49 14.71	-47 54 45.6	09 49 16.53	-47 55 12.9	0.0064	111.73	32.86	4.33	0.59
94	SN2013bl*	08 46 15.06	+41 34 40.0	08 46 14.07	+41 34 47.5	0.0304	62.83	13.40	8.15	0.43
95	SN2013eu*	14 33 58.97	+40 14 20.7	14 33 59.00	+40 14 40.0	0.0252	67.32	19.30	9.80	0.57
96	SN2013ep*	22 58 30.35	+40 25 44.5	22 58 29.31	+40 25 46.3					
97	SN2013fq*	19 59 07.95	-55 55 46.6	19 59 06.40	-55 55 41.6					
98	SN2014cq*	09 23 29.55	-63 40 28.3	09 23 26.79	-63 40 45.3	0.0110	109.18	25.02	5.64	0.46
99	SN2014ds*	08 11 16.45	+25 10 47.4	8 11 15.92	+25 10 45.7	0.0137	44.48	7.39	2.07	0.33
100	SN2015au*	22 30 59.42	-13 59 56.1	22 30 59.91	-14 00 12.8	0.0160	122.50	18.16	5.92	0.30
101	SN2015Y*	09 02 37.87	+25 56 04.2	09 02 38.64	+25 56 04.5	0.0080	84.75	10.39	1.71	0.25
102	SN2016avh*	10 25 47.80	-11 25 17.6	10 25 48.97	-11 25 28.5	0.0380	43.47	20.36	15.35	0.94
103	SN2016bas*	07 38 05.53	-55 11 47.0	07 38 05.53	-55 11 26.7	0.0090	128.28	20.30	3.75	0.32
104	SN2016bhr*	14 25 20.58	+32 28 55.9	14 25 20.59	+32 28 56.5	0.0139	32.97	0.61	0.17	0.04
105	SN2016blq*	11 08 55.51	-29 01 26.4	11 08 55.52	-29 01 25.5					
106	SN2016blt*	14 15 45.76	-47 38 15.0	14 15 45.64	-47 38 27.7	0.0160	79.10	12.76	4.16	0.32
107	SN2016bmd*	07 20 24.3	+32 51 01.2	07 20 24.60	+32 50 58.8					
108	SN2016dsb*	01 58 59.71	-32 22 18.5	01 59 00.57	-32 22 25.2	0.0212	36.15	5.81	2.49	0.32
109	SN2016exv*	03 39 34.38	+20 42 30.4	03 39 34.78	+20 42 31.9	0.0219	36.15	8.70	3.85	0.48
110	SN2016hkn*	02 08 34.23	+29 14 11.1	02 08 34.37	+29 14 02.6	0.0127	49.91	18.71	4.86	0.75
111	SN2016iyc*	22 09 14.20	+21 31 17.5	22 09 15.30	+21 31 06.8	0.0180	90.81	26.67	9.75	0.59
112	SN2016iye*	07 45 19.72	-71 24 17.9	07 45 15.96	-71 24 37.6	0.0360	27.43	13.71	9.81	1.00
113	SN2016M*	07 16 37.75	+67 53 32.3	07 16 36.07	+67 53 42.2	0.0740	21.78	3.64	5.12	0.33
114	SN2016U*	10 34 19.27	+03 24 25.5	10 34 19.10	+03 24 22.9	0.0131	28.72	38.38	10.27	2.67
115	SN2017atu*	09 49 56.70	+67 10 59.6	09 49 50.40	+67 11 11.0	0.0200	23.34	6.52	2.64	0.56
116	SN2017cao*	19 24 02.19	+42 17 21.1	19 24 02.15	+42 17 27.6					
117	SN2017dgd*	16 45 38.967	+01 37 19.7	16 45 39.02	+01 37 13.1	0.0470	45.51	11.18	10.31	0.49
118	SN2017ey*	23 49 28.27	-30 25 04.7	23 49 28.64	-30 25 14.8	0.0330	49.91	8.24	5.43	0.33
119	SN2017fek*	20 21 47.44	-10 43 53.3	20 21 47.70	-10 43 46.0	0.0245	51.07	7.17	3.54	0.28
120	SN2017gfh*	20 03 27.40	+06 59 27.2	20 03 27.78	+06 59 22.8	0.0600	18.54	9.07	10.52	0.98
121	SN2017gfz*	00 12 51.89	-32 43 53.0	00 12 51.80	-32 44 02.0	0.0049	154.22	12.13	1.23	0.16
122	SN2017gkk*	09 13 44.37	+76 28 42.4	09 13 43.04	+76 28 31.2	0.0380	28.72	2.40	1.81	0.17
123	SN2017gth*	01 12 38.19	+05 45 58.4	01 12 38.20	+05 45 56.0	0.0120	39.64	29.73	7.30	1.50
124	SN2017hyh*	07 10 41.07	+06 27 41.4	07 10 40.48	+06 27 13.0	0.0240	27.43	13.02	6.30	0.95
125	SN2017ixz*	07 47 03.03	+26 46 25.8	07 47 02.32	+26 46 34.7	0.0285	19.42	7.90	4.52	0.81
126	SN2017iyl*	11 46 25.00	+01 59 33.1	11 46 24.70	+01 59 39.6	0.0151	49.91	21.53	6.63	0.86
127	SN2017jbl*	03 33 12.73	+36 11 24.6	03 33 13.19	+36 11 03.8	0.0317	45.51	14.59	9.24	0.64
128	SN2017jdn*	10 23 45.51	+53 06 20.5	10 23 46.90	+53 06 28.0					
129	SN2017jo*	09 57 36.150	-22 10 23.91	09 57 36.41	-22 10 30.7	0.0117	57.30	7.04	1.69	0.25
130	SN2017mw*	09 57 20.97	-41 35 21.0	09 57 20.90	-41 35 28.0	0.0339	58.63	7.17	4.85	0.24
131	SN2018arx*	14 06 34.81	-32 34 44.1	14 06 35.05	-32 34 37.6	0.0217	58.63	8.49	3.73	0.29
132	SN2018bsg*	10 10 28.16	+02 13 48.8	10 10 27.86	+02 13 41.6	0.0146	82.82	2.24	0.67	0.05
133	SN2018ddr*	13 58 38.47	+07 13 01.2	13 58 38.56	+07 12 59.4					
134	SN2018dfg*	14 06 34.70	-05 27 02.9	14 06 34.89	-05 27 10.7	0.0095	137.45	8.30	1.62	0.12

135	SN2018fcx*	04 05 56.72	-15 08 43.6	04 05 55.90	-15 08 58.9	0.0250	46.57	19.37	9.75	0.83
136	SN2018fex*	03 55 20.77	-56 45 14.6	03 55 21.66	-56 44 46.6	0.0243	37.86	28.94	14.18	1.53
137	SN2018fpb*	23 59 42.80	+34 20 39.9	23 59 42.96	+34 20 42.6	0.0148	32.22	3.35	1.01	0.21
138	SN2018gj*	16 32 02.31	+78 12 40.9	16 32 39.20	+78 11 53.5	0.0046	134.32	122.64	11.65	1.83
139	SN2018hhs*	23 49 58.18	+07 04 23.7	23 49 58.17	+07 04 19.7					
140	SN2018hqu*	12 16 33.78	+41 31 56.5	12 16 33.76	+41 31 56.0	0.0500	28.72	0.55	0.54	0.04
141	SN2018hyw*	08 20 17.38	+20 52 32.2	08 20 16.57	+20 52 30.3	0.0168	42.48	11.51	3.93	0.54
142	SN2018iuq*	07 05 53.44	+12 53 34.7	07 05 53.41	+12 53 36.8					
143	SN2018jak*	09 59 18.19	+34 53 43.8	09 59 18.13	+34 53 53.3	0.0385	38.74	9.53	7.27	0.49
144	SN2018jee*	07 23 14.632	+56 31 30.45	07 23 14.45	+56 31 29.6					
145	SN2018mc*	18 01 00.832	+61 41 46.92							
146	SN2018ow*	02 51 04.410	+09 06 44.32	02 51 04.80	+09 06 64.3					
147	SN2019abp*	16 23 26.53	+22 29 10.1	16 23 26.24	+22 29 08.6	0.0376				
148	SN2019abp*	16 23 26.534	+22 29 10.11	16 23 26.21	+22 29 08.6					
149	SN2019abp*	16 23 26.534	+22 29 10.11	16 23 26.21	+22 29 08.6					
150	SN2019ail*	10 28 27.28	+12 42 21.8	10 28 27.32	+12 42 14.6	0.0323	68.89	7.22	4.66	0.21
151	SN2019aur*	03 01 10.42	+41 23 45.8	03 01 10.15	+41 23 46.7	0.0124	43.47	3.17	0.80	0.15
152	SN2019bao*	10 29 18.52	+06 07 21.8	10 29 15.50	+06 07 40.8	0.0119	109.18	48.88	11.90	0.90
153	SN2019bzo*	15 55 34.45	+26 54 54.8	15 55 34.46	+26 54 54.0	0.0650				
154	SN2019daf*	13 47 48.12	+72 03 00.4	13 47 48.56	+72 02 59.8	0.0350	33.74	2.12	1.48	0.13
155	SN2019eev*	09 57 05.86	+08 04 10.17	09 57 05.86	+08 04 10.17					
156	SN2019eff*	16 33 39.14	+13 54 36.6	16 33 39.23	+13 54 23.6	0.0500	15.42	13.07	12.77	1.69
157	SN2019fco*	10 32 04.72	+46 55 03.6	10 32 04.34	+46 55 03.8	0.0406	20.33	3.90	3.13	0.38
158	SN2019fks*	21 41 16.50	-16 53 23.0	21 41 16.80	-16 53 23.0	0.0500	18.12	4.31	4.21	0.48
159	SN2019gaf*	20 36 55.23	+02 48 24.6	20 36 54.90	+02 48 14.0	0.0060	31.49	11.70	1.45	0.74
160	SN2019ijj*	14 56 33.53	-25 50 10.9	14 56 33.62	-25 50 06.9	0.0290	33.74	4.18	2.43	0.25
161	SN2019ltw*	16 18 38.54	+21 58 22.9	16 18 38.53	+21 58 24.0	0.0161	35.33	1.11	0.36	0.06
162	SN2019rn*	02 17 59.61	+14 32 00.4	02 17 59.65	+14 32 38.2	0.0131	114.33	37.80	10.12	0.66
163	SN2019xt*	14 11 55.741	-00 50 11.77	14 11 55.78	-00 50 12.0					
164	SNhunt268*	01 14 26.82	+42 33 18.4	01 14 26.27	+42 33 22.6	0.0197	77.29	7.39	2.95	0.19
165	ASASSN-15qz*	01 25 36.09	-41 27 55.8	01 25 35.80	-41 27 55.5	0.0216	36.15	3.27	1.43	0.18
166	CSS151130 ¹	01 42 58.44	+27 34 10.5	01 42 57.60	+27 34 53.0					
167	DES16S1kt*	02 51 07.54	+00 01 33.0	02 51 07.77	+00 01 30.8	0.0675	13.75	4.09	5.29	0.60
168	iPTF13efs*	07 55 26.19	+52 48 17.9	07 55 25.98	+52 48 24.7	0.0408	29.39	7.06	5.69	0.48
169	LSQ12hbo*	10 56 16.00	-20 51 32.0	10 56 12.97	-20 51 10.1	0.0122	79.10	47.79	11.93	1.21
170	LSQ12htu*	10 11 37.11	-07 23 11.6	10 11 37.68	-07 23 15.2	0.0520	21.29	9.21	9.34	0.87
171	LSQ13bca*	21 16 16.39	-20 30 48.9	21 16 16.80	-20 30 54.0	0.0800	25.01	7.69	11.62	0.62
172	LSQ14hj*	13 25 08.05	-32 37 32.8	13 25 07.90	-32 37 31.0	0.0500	22.81	2.61	2.55	0.23
173	LSQ15rw*	14 32 31.33	-13 39 27.4	14 32 31.19	-13 39 26.0	0.0210	43.47	2.47	1.05	0.11
174	OGLE16ekf*	04 37 36.66	-71 48 17.4							
175	PS1-14od*	03 21 06.23	-07 16 57.4	03 21 06.08	-07 16 56.8	0.0200	19.87	2.31	0.94	0.23
176	PS15api*	18 28 58.24	+22 54 10.6	18 28 57.36	+22 54 11.0	0.0140	56.00	12.17	3.48	0.43
177	PS15bgt*	22 46 05.04	-10 59 48.4	22 46 03.70	-11 00 04.3	0.0089	125.36	25.34	4.63	0.40
178	PS15bqc*	17 04 32.29	+01 20 58.5	17 04 32.26	+01 20 47.7	0.0230	37.00	10.81	5.02	0.58
179	PTF10htz*	13 08 37.52	+79 47 13.2	13 08 37.55	+79 47 13.3	0.0352	28.06	0.13	0.09	0.01

⁺ The value of D25 is measured as isophotal level of 25 mag arcsec⁻² in the SDSS g-band (Hakobyan et al. 2012, 2016).

^{*} Candidates to Type IIb Supernovae.

¹ CSS151130:014258+273410

This paper has been typeset from a \LaTeX file prepared by the author.